J. Fluid Mech. (2005), *vol.* 522, *pp.* 117–139.
DOI: 10.1017/S0022112004001715 Printed in the United Kingdom

Nested toroidal vortices between concentric cones

By CHETAN P. MALHOTRA[1], PATRICK D. WEIDMAN[2] AND ANTHONY M. J. DAVIS

[1]Tata Research Development and Design Centre, Pune, India

[2]Department of Mechanical Engineering, University of Colorado, Boulder, CO 80309-0427, USA

[3]Department of Mathematics, University of Alabama, Tuscaloosa, AL 35487-0350, USA

(Received 20 April 2004 and in revised form 5 August 2004)

A few decades ago, the significance of Moffatt vortices was demonstrated by establishing their existence in various flows. Wedge and cusp regions and their axisymmetric counterparts were preferred to conical regions because the associated analyses were simpler. The lowest even and odd modes were always dominant and the streamline patterns of higher modes were assumed to be similarly simple, especially as their minute strength caused computational difficulties. Here, armed with far more computer power, we return to the vortices' canonical structure, with our principal focus on the region exterior to two cones with common axis and vertex. Many interesting features are revealed, the most unexpected being the structure of the third (second odd in a symmetric geometry) mode. The two-cone geometry allows consideration of asymmetric regions, for the first time. Comparisons are made with the well-known wedge and single-cone results and numerical corrections made to the latter. In all cases, eigenvalue plots play a valuable role in guiding the discussion.

1. Introduction

Ever since the paper by Dean & Montagnon (1949) and the studies by Moffatt (1964), Moffatt & Duffy (1980), and Liu & Joseph (1978), there has been considerable interest in the low-Reynolds-number motion in wedges and cones, showing the existence of a sequence of counter-rotating eddies into the vertex. The wedge and cone geometries admit separation-of-variables analysis of the Stokes flow equations. Solutions of this type, however, are not just of fundamental interest. Davis (1989) models the thermocapillary flow in the floating zone method of crystal growth as a Stokes problem in the corner between the solid crystal and the liquid melt with various surface stress conditions. A similar analysis for the wedge geometry was reported by Kuhlmann, Nienhüser & Rath (1999) for a constant thermocapillary stress. Stokes solutions have also been used to predict the morphology of soft moulded objects released from their matrix in wedge (Betelú *et al.* 1996) and cone (Weidman & Calmidi 1999) geometries.

In the present study, Stokes flow in a geometry distinctly different from the wedge or conical trench is investigated. Motivation is given in figure 1 which depicts two low-Reynolds-number stagnation flows. Figure 1(*a*) shows a two-dimensional stagnation flow impinging normally on a cylinder placed on a horizontal wall; the separated flow over the cylinder results in a nested vortex structure in the cusped regions between the cylinder and the wall. Though the cylinder is curved, a simple model for

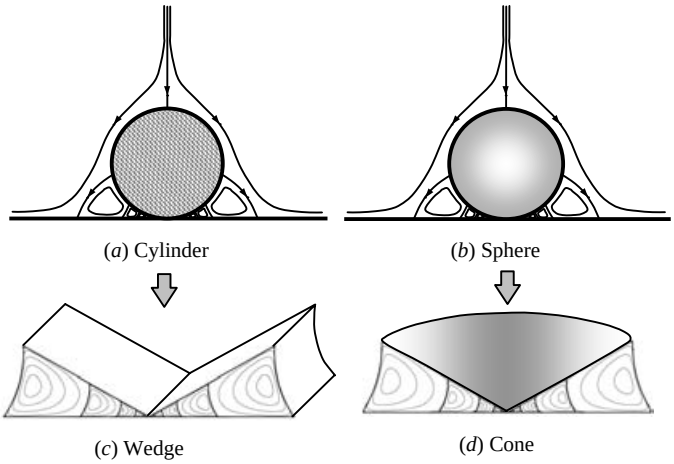

FIGURE 1. Schematic diagrams of streamline patterns for (*a*) planar stagnation-point flow impinging on a cylinder resting on a plane and (*b*) axisymmetric stagnation-point flow impinging on a sphere resting on a plane. Model geometries to study the nested vorticies in (*a*) and (*b*) are respectively the flow (*c*) between intersecting planes and the flow (*d*) between intersecting cones.

the corner flow is given by Moffatt's (1964) sequence of eddies formed in a planar wedge composed of intersecting flat planes shown in figure 1(*c*). Figure 1(*b*) shows the nested toroidal vortex structure reported by Davis & O'Neill (1977*a*) for axisymmetric Stokes stagnation flow impinging normally on a sphere placed on a horizontal wall. By analogy with the cylinder problem, a simple model of the flow in the axisymmetric cusp region is the corner flow in the axisymmetric wedge bounded by a cone and the horizontal plane it touches, as shown in figure 1(*d*). Referring to figure 3 below, it is clear that the horizontal wall in figure 1(*d*) is the particular case, $\theta_2 = \pi/2$, of the second of two coaxial cones having a common vertex, with semi-vertex polar angles θ_1 and θ_2.

Pursuant to this study we found that the separatrices between nested eddies are never conical above mode number two. This motivates a further investigation of the shape of separatrices between nested eddies in the simpler wedge geometry where non-trivial boundaries between the nested eddies are also found at elevated mode number. Another aspect of the work reported here results from testing our numerical code in solving the eigenvalue equation derived by Liu & Joseph (1978) for Stokes flow in a conical trench of apex angle $2\theta_0$; we discovered that the Liu & Joseph computations are in error, and their reported critical angle for the disappearance of nested vortices is different from the value 80.9° reported earlier by Wakiya (1976). Corrections to their published eigenvalues for selected values of θ_0 and a sample streamline plot are provided in this paper.

The presentation is organized as follows. Essential for understanding our results, we briefly review in § 2 the findings of Moffatt (1964) for the classic eigenvalue problem and introduce our notation for even and odd eigenvalues. Derivation of the eigenvalue problem for flow between concentric cones is given in § 3. New results for symmetric flows and their connection to the classic wedge problem given in § 3.1 are followed by a presentation of results for asymmetric flows in § 3.2. The reduction to the single-cone problem and computations correcting the results of Liu & Joseph (1978) are given in § 4. Concluding remarks are given in § 5.

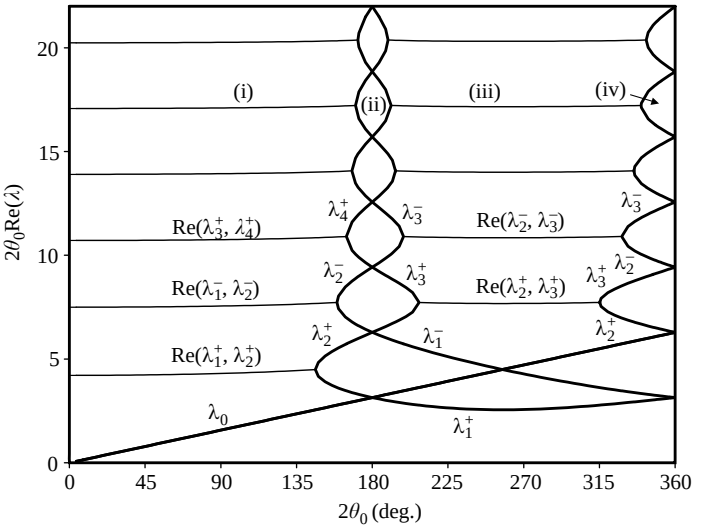

FIGURE 2. Eigenvalue distribution for the lowest even and odd modes for the wedge problem showing the four distinct regions (i), (ii), (iii) and (iv) that appear.

2. Review of the Moffatt problem

It will be shown that similarities exist between vortex structures situated between cones symmetrically opening about the equator, and those situated between intersecting planes. Following Moffatt (1964) we denote by $2\theta_0$ the included angle between intersecting planes and define $\Delta\theta = \theta_2 - \theta_1$ to be the 'latitude' angle between cones. For intersecting planes, fluid fills the entire spatial domain when $2\theta_0 = 2\pi$ and so the available range of wedge openings is $0 < 2\theta_0 < 2\pi$. For the double-cone configuration, fluid fills the entire spatial domain when $\Delta\theta = \pi$ and hence the available range of included angles in this situation is $0 < \Delta\theta < \pi$.

Moffatt (1964) showed that the eigenvalues for Stokes solutions $\psi = \mathrm{Re}[r^{\lambda+1} f(\theta)]$ describing planar flow in a wedge, provided $\mathrm{Re}(\lambda) > 0$, must be computed from separate eigenvalue equations, namely

$$\sin(2\lambda\theta_0) \pm \lambda \sin 2\theta_0 = 0 \qquad (\lambda \neq 1) \tag{1}$$

where the positive sign is for odd modes and the negative sign for even modes. Figure 2 shows the distribution of the computed real parts of $2\theta_0\lambda^{\pm}$ for odd and even modes, wherein the labelling sequence $\pm$ is used in accordance with (1) and the range of wedge angles extends to the 'knife edge' $2\theta_0 = 360^\circ$. The canonical form of equation (1) is $\sin z \pm z(\sin 2\theta_0/2\theta_0) = 0$ where $z = 2\lambda\theta_0$. As $\theta_0 \to 0$, this equation gives

$$\sin z \pm z = 0 \tag{2}$$

and the limiting values of $2\lambda\theta_0$, listed for example by Davis & O'Neill (1977*b*), are plotted as solid circles on the vertical axis in figure 2. Note that the $\theta_0 = 0$ ordinate values are approached horizontally because $\sin 2\theta_0/2\theta_0 = 1 - O(\theta_0^2)$.

The four regions (i)–(iv) discerned in figure 2 constitute different flow structures in the wedge: (i) nested vortices, (ii) first region void of vortices, (iii) double vortices pinned to the origin, and (iv) a second region void of vortices. These regions owe their existence to that of real eigenvalues on either side of 180° and as 360° is approached. Bifurcations between pairs of real and complex-conjugate eigenvalues are evident

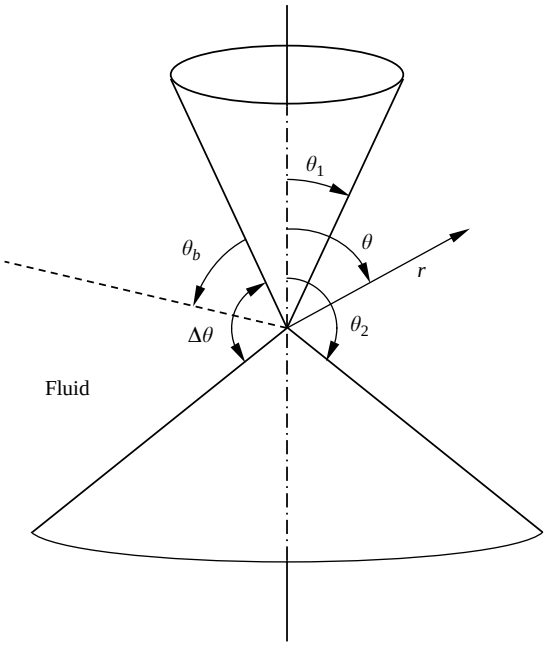

FIGURE 3. Spherical coordinate system (r, θ) showing cone boundaries θ_1 and θ_2, the included angle $\Delta\theta$ between cones and the angle θ_b bisecting the fluid region between cones.

and, if the disallowed solution, $\lambda = \lambda_0 = 1$, of $\sin(2\lambda\theta_0) - \lambda \sin 2\theta_0 = 0$ is included, the eigenvalues of the two equations in (1) coincide at 180°, where the curves cross, and at 360°. Here, and in what follows, we label in ascending order the real solutions of each equation in region (ii) on the left (lower) side of 180°. Evidently, the pairings of complex-conjugate eigenvalues in region (iii) differ from those in region (i). For example, the curve labelled $\mathrm{Re}(\lambda_1^+, \lambda_2^+)$ in (i) bifurcates into λ_1^+, which remains real through to 360°, and into λ_2^+, which crosses λ_1^- at 180° and subsequently joins λ_3^+ on the path labelled $\mathrm{Re}(\lambda_2^+, \lambda_3^+)$ across region (iii) before becoming real in region (iv). Similar comments apply to the curve labelled $\mathrm{Re}(\lambda_1^-, \lambda_2^-)$ in (i) and the ensuing 'change of partners' structure is established. Remarkably, the eigenplot for two cones symmetric about the equator yields an eigenvalue structure very similar to regions (i) and (ii) in figure 2, and the associated streamline plots presented in § 3.1 exhibit similar features to those of the wedge.

3. The double-cone eigenvalue problem

Axisymmetric incompressible flow with zero swirl velocity is assumed. The fluid density and kinematic viscosity are constant. Spherical polar coordinates (r, θ) are employed and the fluid is located between two concentric cones with semivertex angles θ_1 and $\theta_2 (> \theta_1)$, as sketched in figure 3, which also shows the opening angle $\Delta\theta$ and its bisector θ_b. Velocity components along the direction of the unit vectors $(\boldsymbol{e}_r, \boldsymbol{e}_\theta)$ are denoted by (u, v), respectively. For the divergence-free flow, a Stokes streamfunction $\Psi(r, \theta)$ exists and is related to the velocity components according to

$$u = \frac{1}{r^2 \sin\theta} \frac{\partial \Psi}{\partial \theta}, \qquad v = -\frac{1}{r \sin\theta} \frac{\partial \Psi}{\partial r}. \tag{3}$$

For Stokes flow the fluid motion is governed by the fourth-order equation

$$\mathrm{L}_{-1}^2\Psi = \left[\frac{\partial^2}{\partial r^2} + \frac{1-\xi^2}{r^2}\frac{\partial^2}{\partial \xi^2}\right]^2 \Psi = 0, \tag{4}$$

where L_{-1} denotes the Stokes operator and $\xi = \cos\theta$. Liu & Joseph (1978) have shown that explicit eigenfunctions for this problem are readily obtained by separating variables according to $\Psi(r,\theta) = \mathrm{Re}[r^{\mu+3/2} f_\mu(\xi)]$, but it is simpler if one anticipates the $r^2\sin^2\theta$ factor in Ψ by writing

$$\Psi(r,\theta) = \mathrm{Re}\left[r^{\mu+3/2}(1-\xi^2)F_\mu(\xi)\right], \tag{5}$$

where $\mathrm{Re}(\mu) > 1/2$. Then F_μ is easily determined by successively solving the equations

$$\frac{\mathrm{d}^2}{\mathrm{d}\xi^2}[(1-\xi^2)E_\mu] + \left(\mu - \tfrac{1}{2}\right)\left(\mu - \tfrac{3}{2}\right)E_\mu = 0, \quad \frac{\mathrm{d}^2}{\mathrm{d}\xi^2}[(1-\xi^2)F_\mu] + \left(\mu + \tfrac{1}{2}\right)\left(\mu + \tfrac{3}{2}\right)F_\mu = E_\mu, \tag{6}$$

to obtain the general solution, for $\mu \neq \frac{3}{2}$,

$$F_\mu(\xi) = A\,P'_{\mu+1/2}(\xi) + B\,P'_{\mu-3/2}(\xi) + C\,Q'_{\mu+1/2}(\xi) + D\,Q'_{\mu-3/2}(\xi) \tag{7}$$

where a prime denotes differentiation of a Legendre function. The use of μ instead of the more obvious $k + \frac{1}{2}$ is primarily for easy comparison with the results of Liu & Joseph (1978), but turns out to be the optimal choice for discussing the limit $\Delta\theta \to 0$. Impermeable and no-slip boundary conditions apply at each solid surface $\theta = \theta_1, \theta_2$ bounding the fluid. Thus, according to (3) and (5)

$$F_\mu(\xi_1) = F_\mu(\xi_2) = 0, \qquad F'_\mu(\xi_1) = F'_\mu(\xi_2) = 0 \tag{8}$$

where $\xi_1 = \cos\theta_1$ and $\xi_2 = \cos\theta_2$. The four homogeneous boundary conditions give rise to the eigenvalue problem determining μ in the first quadrant of the complex plane, namely

$$\begin{vmatrix} P'_{\mu+1/2}(\xi_1) & P'_{\mu-3/2}(\xi_1) & Q'_{\mu+1/2}(\xi_1) & Q'_{\mu-3/2}(\xi_1) \\ P'_{\mu+1/2}(\xi_2) & P'_{\mu-3/2}(\xi_2) & Q'_{\mu+1/2}(\xi_2) & Q'_{\mu-3/2}(\xi_2) \\ P''_{\mu+1/2}(\xi_1) & P''_{\mu-3/2}(\xi_1) & Q''_{\mu+1/2}(\xi_1) & Q''_{\mu-3/2}(\xi_1) \\ P''_{\mu+1/2}(\xi_2) & P''_{\mu-3/2}(\xi_2) & Q''_{\mu+1/2}(\xi_2) & Q''_{\mu-3/2}(\xi_2) \end{vmatrix} = 0. \tag{9}$$

For each mode $\mu_n (n = 1, 2, 3\ldots)$, the radial and polar velocities computed from (3) are

$$u_n(r,\xi) = \mathrm{Re}\left\{-r^{\mu_n - 1/2}[(1-\xi^2)F_{\mu_n}]'\right\}, \tag{10a}$$

$$v_n(r,\xi) = (1-\xi^2)^{1/2}\mathrm{Re}\left[-(\mu_n + 3/2)r^{\mu_n - 1/2}F_{\mu_n}(\xi)\right]. \tag{10b}$$

Complex roots of equation (9) were found using the modified secant method in Mathematica (Wolfram 1991). In order to generate the eigenvalue distributions, an outer loop stepped θ_2 keeping θ_1 constant, while an inner loop changed the search window towards higher eigenvalues. In spite of the advancing window, the search often ended at a previously calculated eigenvalue. To prevent repetition, a table of eigenvalues was maintained, and successively computed eigenvalues were added to the table if found to be new. Furthermore, to filter out spurious eigenvalues, each new eigenvalue was resubstituted in equation (9) and accepted only when its right-hand side was within an acceptable tolerance, typically 10^{-3}.

3.1. *Symmetric flow region*

The particular case $\theta_1 = (\pi - \Delta\theta)/2$, $\theta_2 = (\pi + \Delta\theta)/2$ has a fluid region that is symmetric about the plane $\theta = \pi/2$, that is $\xi = 0$. The relations

$$P'_\nu(-\xi) = -\cos\nu\pi P'_\nu(\xi) + \frac{2}{\pi}\sin\nu\pi Q'_\nu(\xi),$$

$$Q'_\nu(-\xi) = \cos\nu\pi Q'_\nu(\xi) + \frac{\pi}{2}\sin\nu\pi P'_\nu(\xi),$$

(Gradshteyn & Ryzhik 1994, section 8.737) imply that

$$G_\nu(\xi) = \cos\frac{\nu\pi}{2} Q'_\nu(\xi) + \frac{\pi}{2}\sin\frac{\nu\pi}{2} P'_\nu(\xi) \tag{11}$$

is an even function of ξ while

$$g_\nu(\xi) = \sin\frac{\nu\pi}{2} Q'_\nu(\xi) - \frac{\pi}{2}\cos\frac{\nu\pi}{2} P'_\nu(\xi) \tag{12}$$

is an odd function of ξ. Thus

$$F_\mu(\xi) = A\, G_{\mu+1/2}(\xi) + B\, G_{\mu-3/2}(\xi) \tag{13}$$

is a symmetric solution provided

$$\begin{vmatrix} G_{\mu+1/2}(\xi_0) & G_{\mu-3/2}(\xi_0) \\ \dfrac{\mathrm{d}}{\mathrm{d}\xi} G_{\mu+1/2}(\xi_0) & \dfrac{\mathrm{d}}{\mathrm{d}\xi} G_{\mu-3/2}(\xi_0) \end{vmatrix} = 0, \tag{14}$$

where $\xi_0 = \sin(\Delta\theta/2)$. Similarly,

$$F_\mu(\xi) = C\, g_{\mu+1/2}(\xi) + D\, g_{\mu-3/2}(\xi) \tag{15}$$

is an antisymmetric solution provided

$$\begin{vmatrix} g_{\mu+1/2}(\xi_0) & g_{\mu-3/2}(\xi_0) \\ \dfrac{\mathrm{d}}{\mathrm{d}\xi} g_{\mu+1/2}(\xi_0) & \dfrac{\mathrm{d}}{\mathrm{d}\xi} g_{\mu-3/2}(\xi_0) \end{vmatrix} = 0. \tag{16}$$

Equations (14) and (16) can be deduced from (9) by writing the latter in terms of G_ν and g_ν ($\nu = \mu + 1/2$, $\mu - 3/2$) and exploiting the even and odd properties to obtain a product of two 2×2 determinants when $\xi_2 = -\xi_1$.

Careful computations of (14) and (16) established the bifurcating structure of the 'even' and 'odd' eigenvalues presented on the right-hand side of figure 4. The shape of the curves at lower angles, $\Delta\theta$, and in particular their limit points as $\Delta\theta$ goes to zero, indicated that eigenvalues of $\mu\Delta\theta$ should be plotted, corresponding to $2\lambda\theta_0$ in figure 2. However, since $P'_\nu(\xi)$ and $Q'_\nu(\xi)$ become very large at large values of ν as $\xi \to 0$ and 1, respectively, accurate evaluation of the Legendre functions becomes difficult as $\Delta\theta \to 0$. The situation was rescued by noting that the evident monotonic dependence on angle allows the curves to be completed using relaxed linear extrapolation as $\Delta\theta \to 0$, shown by the dashed lines in figure 4.

The combined evolution, which gives $\mathrm{Re}(\mu)\Delta\theta$ as a function of the opening angle $\Delta\theta$, shows only two regions: the primary region (i) of nested vortices at low values of $\Delta\theta$ and region (ii) of no vortices. Though the crossover points occur at less than 180°, region (iii) never appears. The labelling is as in figure 2, with μ instead of λ.

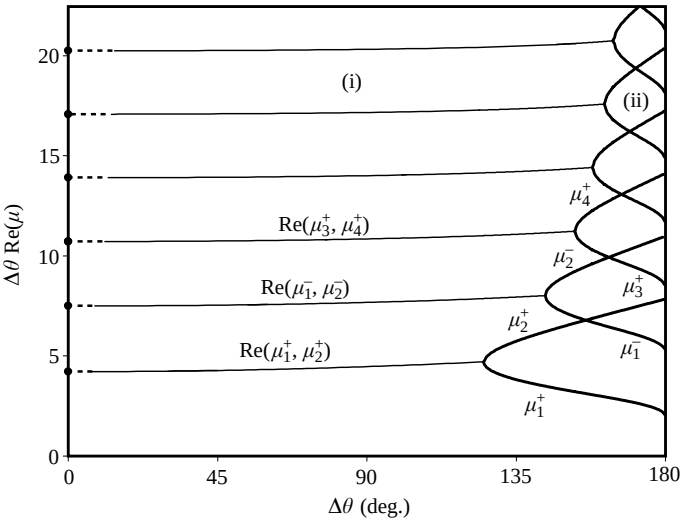

FIGURE 4. Eigenvalue distribution for symmetric cones showing the two distinct regions (i) and (ii) that appear.

It may be deduced from the asymptotic forms for P'_ν, Q'_ν (Gradshteyn & Ryzhik, section 8.721) that the large eigenvalues coincide asymptotically with those of

$$\sin \mu\Delta\theta \pm \mu \sin \Delta\theta = 0, \tag{17}$$

which indicates ultimate agreement with (1) and hence the wedge geometry as $\Delta\theta \to 0$. Consequently, the extrapolated curves in region (i) also terminate at the limit points given by equation (2) with $z = \mu\Delta\theta$ and marked by the filled circles on the vertical axis in figure 4.

Figure 5 displays, for $\Delta\theta = 60^\circ$, the nested vortices in the first three modes of region (i), namely (+1,+2), (−1,−2) and (+3,+4). (Here and in what follows, we use the shorthand notation (+1,+2) for eigenvalues (λ^{+1}, λ^{+2}), and similarly for the μ eigenvalues.) The single vortex in panel (*a*) and the counter-rotating toroidal vortex pair in panel (*b*) are as anticipated, but the nested structure in panel (*c*) is quite unexpected. The vortices above and below the equator rotate in the same direction and one may note the small free vortex rotating in the opposite direction that appears straddling the bisector. All streamline patterns alternate in flow direction and decrease in magnitude as one descends to the apex. For example, the maximum absolute value of the streamfunction for the three topmost vortices in figure 5(*a*) is 0.154, 1.42×10^{-5}, and 1.26×10^{-9}, respectively.

Flows in the wedge and symmetric double-cone geometries have similar streamline patterns. In particular, the third and presumably higher modes have structures unanticipated by earlier authors. Wedge streamline patterns computed for each nested vortex mode (+1,+2), (−1,−2) and (+3,+4) at $2\theta_0 = 60^\circ$ are plotted in figure 6 to compare with the double-cone results for the same modes at $\Delta\theta = 60^\circ$ in figure 5. Note that in both cases a free vortex appears in panel (*c*) and that the radial separatrix between nested vortices for this mode is not a plane for the wedge nor a conical surface for the double cone.

Figure 6 demonstrates that, for the second and higher odd modes, the dividing streamlines are very different from arcs $r = \text{const}$. For the wedge bounded by $\theta = \pm\theta_0$,

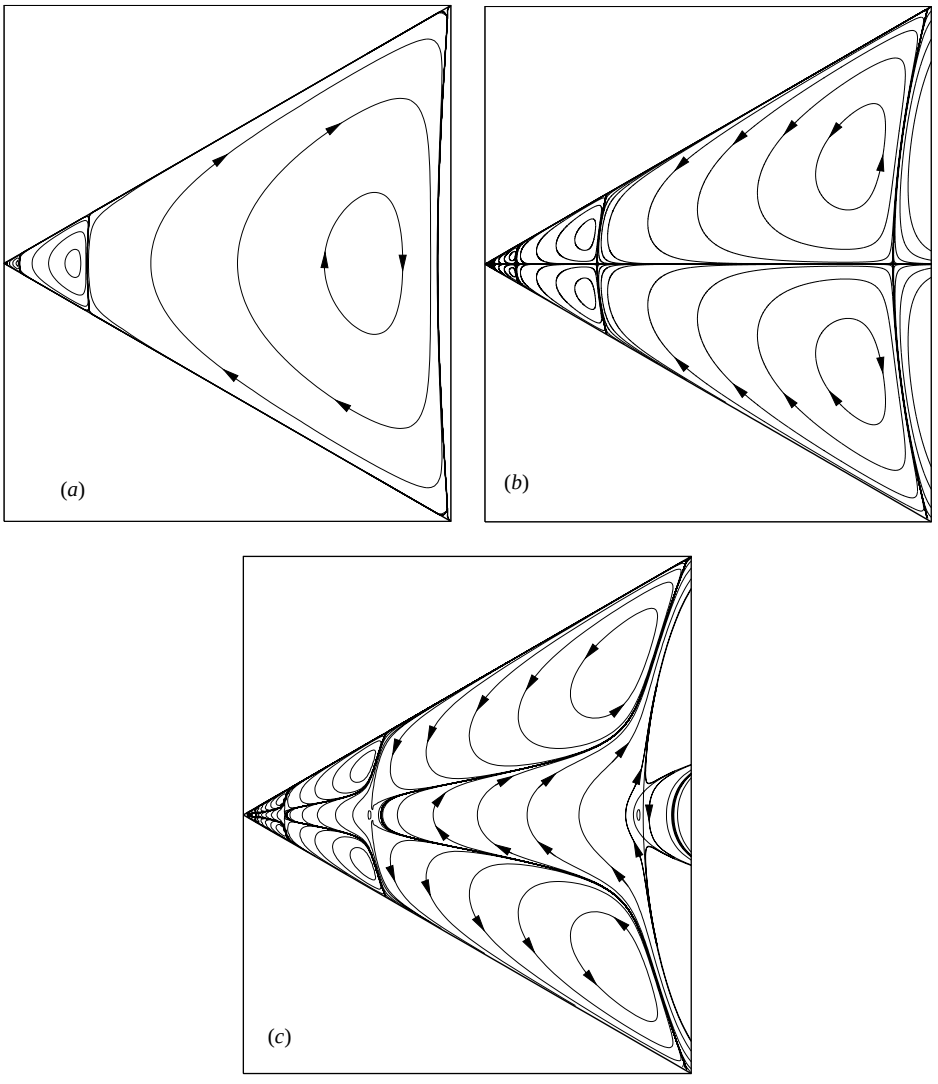

FIGURE 5. Nested vortices for a symmetric opening of the cones at $\Delta\theta = 60^\circ$ for the three lowest modes: (*a*) mode (+1, +2), (*b*) mode (−1, −2), and (*c*) mode (+3, +4).

the streamfunction $\psi = \mathrm{Re}[r^{\lambda+1} f(\theta)]$, where

$$f = \frac{\cos(\lambda+1)\theta}{\cos(\lambda+1)\theta_0} - \frac{\cos(\lambda-1)\theta}{\cos(\lambda-1)\theta_0}, \qquad \lambda \sin 2\theta_0 + \sin 2\lambda\theta_0 = 0, \tag{18}$$

vanishes whenever $\mathrm{Im}(\lambda)\ln r + \arg f(\theta) = (n + 1/2)\pi$ for some integer n. On radial lines $\theta = \text{const.}$, $\psi = 0$ at values of r in geometric progression, as is well-known, but on arcs $r = \text{const.}$, multiple solutions of $\psi = 0$ occur whenever there are angles θ_k, θ_{k+1} such that $f(\theta_k)/f(\theta_{k+1})$ is real and negative and then their positioning depends on the chosen value of r. Similar observations apply to the second and higher even modes, which also have the fixed dividing streamline $\theta = 0$. The limit $\theta_0 = 0$ is illustrated by

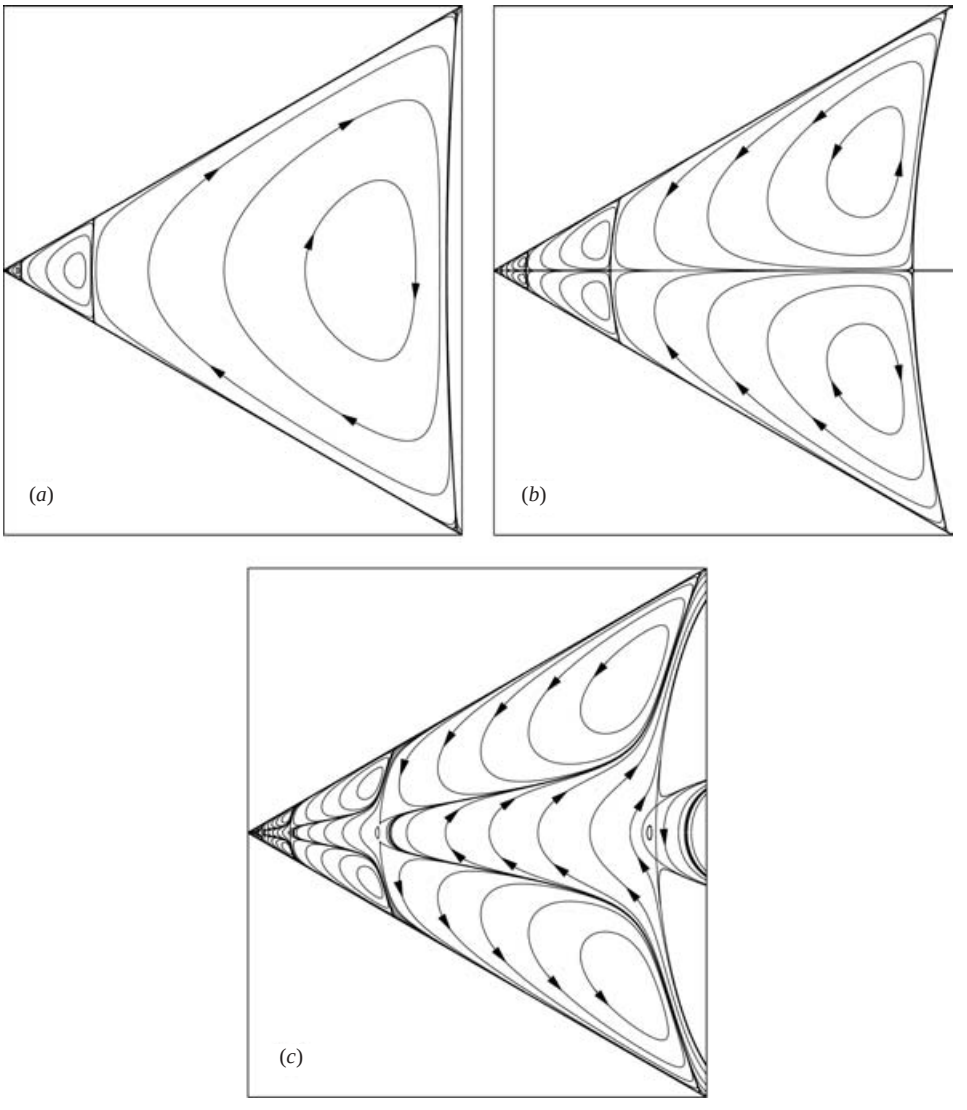

FIGURE 6. Moffatt eddies in a wedge at $2\theta_0 = 60^\circ$ for (*a*) the $(+1, +2)$ mode, (*b*) the $(-1, -2)$ mode, and (*c*) the $(+3, +4)$ mode. Note the striking similarity with the eddies in figure 5 for a symmetric opening $\Delta\theta = 60^\circ$ about the equator.

the exponentially growing channel eigenfunctions,

$$\psi = \mathrm{Re}\left[\left(\frac{x\sin\lambda x}{\sin x} - \frac{\cos\lambda x}{\cos x}\right)\mathrm{e}^{\lambda y}\right], \qquad (|x| < 1,\ \ y > 0), \qquad 2\lambda + \sin 2\lambda = 0, \quad (19)$$

and their odd counterparts.

We explore the topology, evolution and extinction of the free vortex with increasing opening angle in figure 7 by magnifying a $\pm 5^\circ$ segment of the flow centred on the toroidal vortex whose centre circle moves radially outward with increasing $\Delta\theta$. The topology in panel (*a*) for $\Delta\theta = 30^\circ$ consists of the vortex straddling the equator with clockwise circulation, bounded by obliquely impinging streamsurfaces forming free stagnation circles to the north and south. The pattern stretches polewards through

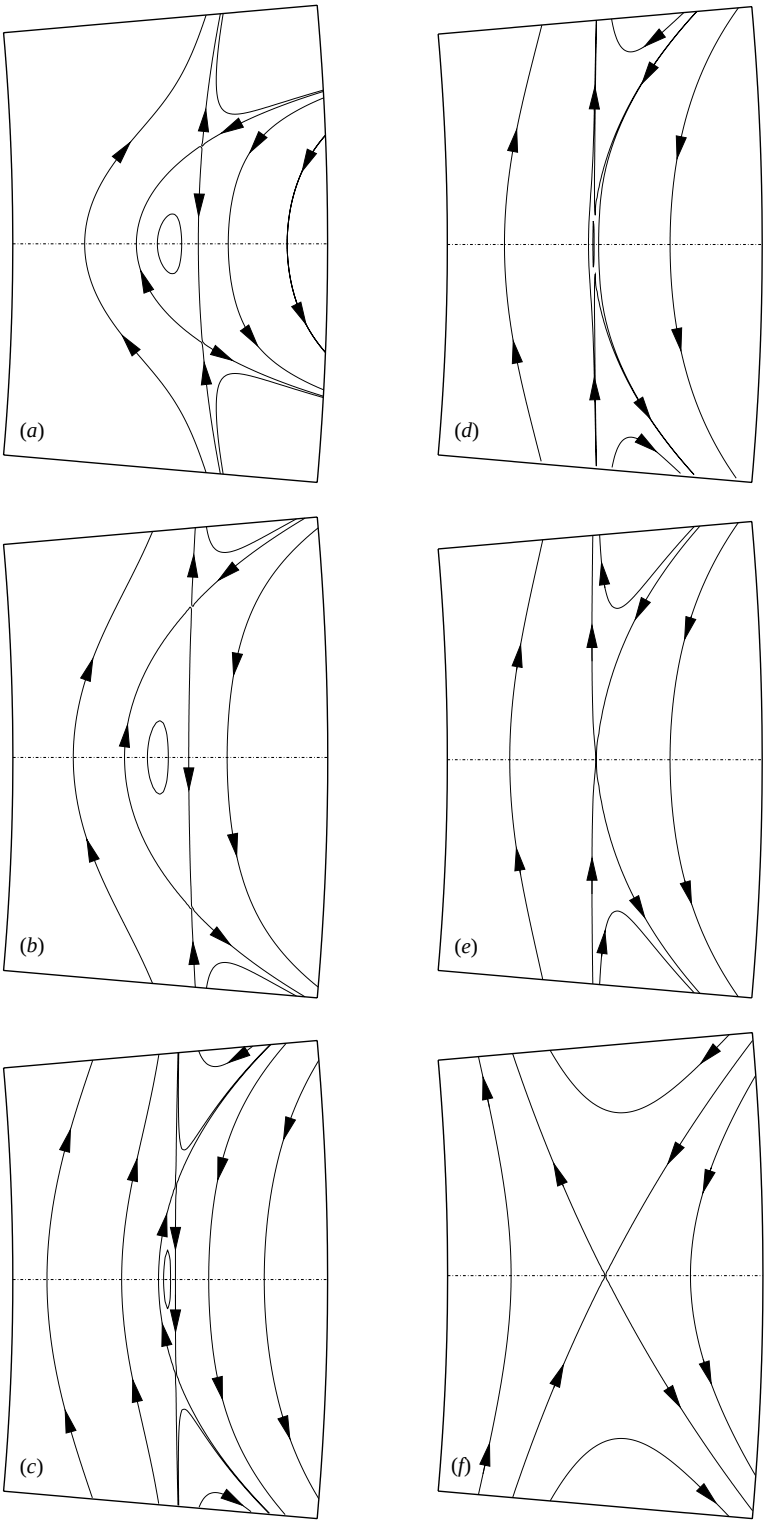

FIGURE 7. Evolution and disappearance of the free vortex for a symmetric opening of the cones; (*a*) $\Delta\theta = 30°$, (*b*) $\Delta\theta = 60°$, (*c*) $\Delta\theta = 82.5°$, (*d*) $\Delta\theta = 87.0°$, (*e*) $\Delta\theta = 90.0°$, (*f*) $\Delta\theta = 150°$.

frame (*b*) at $\Delta\theta = 60^\circ$ and then shrinks through frame (*c*) at $\Delta\theta = 82.5^\circ$ and frame (*d*) at $\Delta\theta = 87^\circ$, with extinction before frame (*e*) where $\Delta\theta = 90^\circ$. This leaves only a single free stagnation circle on the equator in frame (*f*) at $\Delta\theta = 150^\circ$.

3.2. *Asymmetric flow region*

At small values of $\theta_2 - \theta_1 = \Delta\theta$, the eigenvalues become large and thus the asymptotic estimates given by Gradshteyn & Ryzhik (1994, section 8.721), for $\mu\theta \gg 1$, can be used. Since scale factors cancel in the 4×4 determinant set equal to zero, the leading-order terms in (9) yield

$$\begin{vmatrix} \cos[(\mu+1)\theta_1 + \pi/4] & \dots & -\sin[(\mu+1)\theta_1 + \pi/4] & \dots \\ \cos[(\mu+1)\theta_2 + \pi/4] & \dots & -\sin[(\mu+1)\theta_2 + \pi/4] & \dots \\ (\mu+1)\sin[(\mu+1)\theta_1 + \pi/4] & \dots & (\mu+1)\cos[(\mu+1)\theta_1 + \pi/4] & \dots \\ (\mu+1)\sin[(\mu+1)\theta_2 + \pi/4] & \dots & (\mu+1)\cos[(\mu+1)\theta_2 + \pi/4] & \dots \end{vmatrix} \sim 0, \tag{20}$$

in which the second and fourth columns are obtained from the first and third respectively by replacing $\mu + 1$ by $\mu - 1$. The optimal expansion is in terms of six products of 2×2 minors, with the first and third, second and fourth columns paired to keep $\mu + 1$ and $\mu - 1$ separate. Remarkably, the resulting six terms are independent of $\theta_1 + \theta_2$ and pair off to give

$$\begin{aligned} &-[(\mu-1)^2 + (\mu+1)^2]\sin[(\mu+1)\Delta\theta]\sin[(\mu-1)\Delta\theta] \\ &\quad + (\mu^2 - 1)\{2 - 2\cos[(\mu+1)\Delta\theta]\cos[(\mu-1)\Delta\theta]\} \\ &\quad = -2\mu^2\cos[2\Delta\theta] + 2\cos[2\mu\Delta\theta] + 2(\mu^2 - 1) \\ &\quad = 4\mu^2\sin^2(\Delta\theta) - 4\sin^2(\mu\Delta\theta) \sim 0. \end{aligned} \tag{21}$$

In the limit $\Delta\theta \to 0$ and $\mu \to \infty$ this equation becomes exact, factoring into the pair of equations $\sin(\mu\Delta\theta) \pm \mu\sin\Delta\theta = 0$. Identifying $z = \mu\Delta\theta$ again gives equation (2), showing that the wedge, symmetric double-cone (17) and asymmetric double-cone geometries all have the same limits as $\Delta\theta \to 0$.

Despite this odd/even split in the limit of zero angle, the labelling adopted in the symmetric case is inappropriate here. Seeking a corresponding overall count, the left-hand bifurcations are labelled by ascending values of m and the associated eigenvalues by (μ_{m1}, μ_{m2}). When the value of θ_2 yields a symmetric region ($\theta_1 + \theta_2 = 180^\circ$), we then have $(\mu_{m1}, \mu_{m2}) = (\mu_m^+, \mu_{m+1}^+)$ or (μ_{m-1}^-, μ_m^-), according to whether m is odd or even (cf. figure 4).

The eigenvalue distribution for $\theta_1 = 1^\circ$ is given in figure 8. Where complex roots are obtained we plot only the real part as indicated. The solid dots at $\Delta\theta = 0$ indicate the limits mentioned above. At $\theta_1 = 1^\circ$ the eigenvalue distributions are similar to those for a conical trench (figure 15) and of Weidman & Calmidi (1999) for the free-surface cone in the sense that, for $m > 2$ for increasing θ_2, the following sequence similar to that for flow in a wedge (cf. figure 2) is observed: region (i) of nested vortices, region (ii) without vortices, region (iii) exhibiting a solitary vortex, and region (iv) with no vortices up to the highest wedge or cone angle possible. Streamline patterns computed in these four regions, marked by the filled dots in figure 8 are presented in figure 9. The solitary vortex for $\Delta\theta = 149^\circ$ in figure 9(*c*) emanates from the corner, is attached to the lower wall, and does not repeat itself at larger radii.

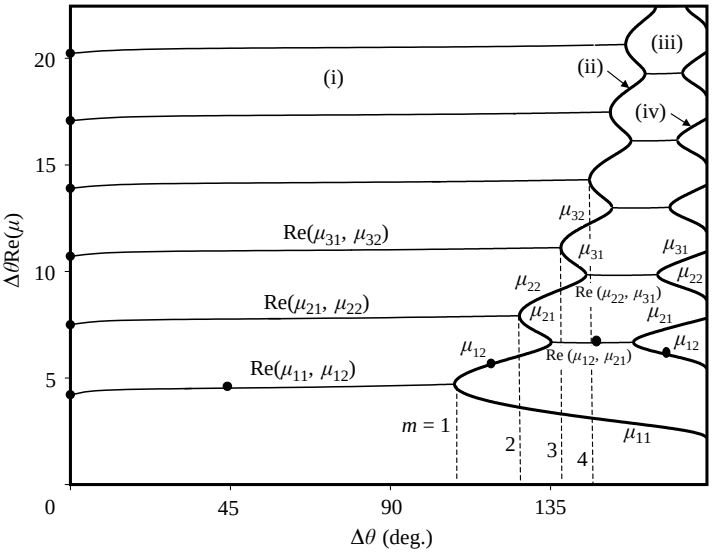

FIGURE 8. Eigenvalue distribution for $\theta_1 = 1°$. The solid points are locations at which streamline plots are made in figure 9.

Figure 8 indicates two interesting contrasts. Whereas the conical trench (figure 15) has region (ii) symmetric about $2\theta_0 = 180°$, it is suggested, and backed by an eigenplot for $\theta_1 = 0.001°$, that the onset of region (ii) as $\theta_1 \to 0°$ (when the upper cone becomes an infinitesimally thin needle) occurs at $\Delta\theta = 90°$. All modes simultaneously become real in this limit (see figure 12*a*). The case $\theta_1 = 90°$, $\theta_2 \to 180°$ exhibits similar features. Secondly, regions (iii) and (iv) appear but are absent from the symmetric case (figure 4). We rationalize this by observing that a symmetric opening about the equator mimics a wedge of angle $<180°$, whereas an asymmetric opening with angle $>90°$, and thus θ_1/θ_2 necessarily small, mimics a wedge of angle $>180°$, which allows flow to come from one direction and bifurcate at the boundary, hence giving flow structures seen only in regions (iii) and (iv).

The evolution of the eigenvalue diagrams with increasing upper cone angles $\theta_1 = 1°$, 10°, 30°, 45°, 60°, 90° and corresponding max $\Delta\theta = 179°$, 170°, 150°, 135°, 120°, 90° are displayed in figure 10. Again, the solid dots on the ordinate are the limiting values obtained from equation (2). In all cases, only vortices exist if $\Delta\theta < 90°$, implying that flow cannot go into and out of the conical wedge. It is seen that successive regions shrink and disappear with increasing θ_1 as follows: first region (iv) shrinks and disappears, next region (iii) shrinks, and then region (ii) shrinks until at $\theta_1 = 90°$ only region (i) of nested vortices remains for all mode numbers m. Actually, using the symmetry inherent in the problem, it can be inferred from the eigenplot for $\theta_1 = 0.001°$ that regions (iii) and (iv) in figure 10(*e*) do not disappear; rather they exist in an infinitesimally thin domain adjacent to $\Delta\theta = 120°$, where the lower cone becomes a needle.

An idea of the complicated asymmetric streamline patterns observed is given in figure 11 which shows the first three modes for $\theta_1 = 10°$ and $\theta_2 = 135°$ corresponding to $\Delta\theta = 125°$ shown as solid dots in figure 10(*b*).

The first non-trivial eigenvalue pair $m = 1$ is of primary interest owing to its dominance over the higher eigenvalues. For each value of θ_1 there is a critical value $(\theta_2)_c$, listed in table 1, marking the transition from region (i) to region (ii) at

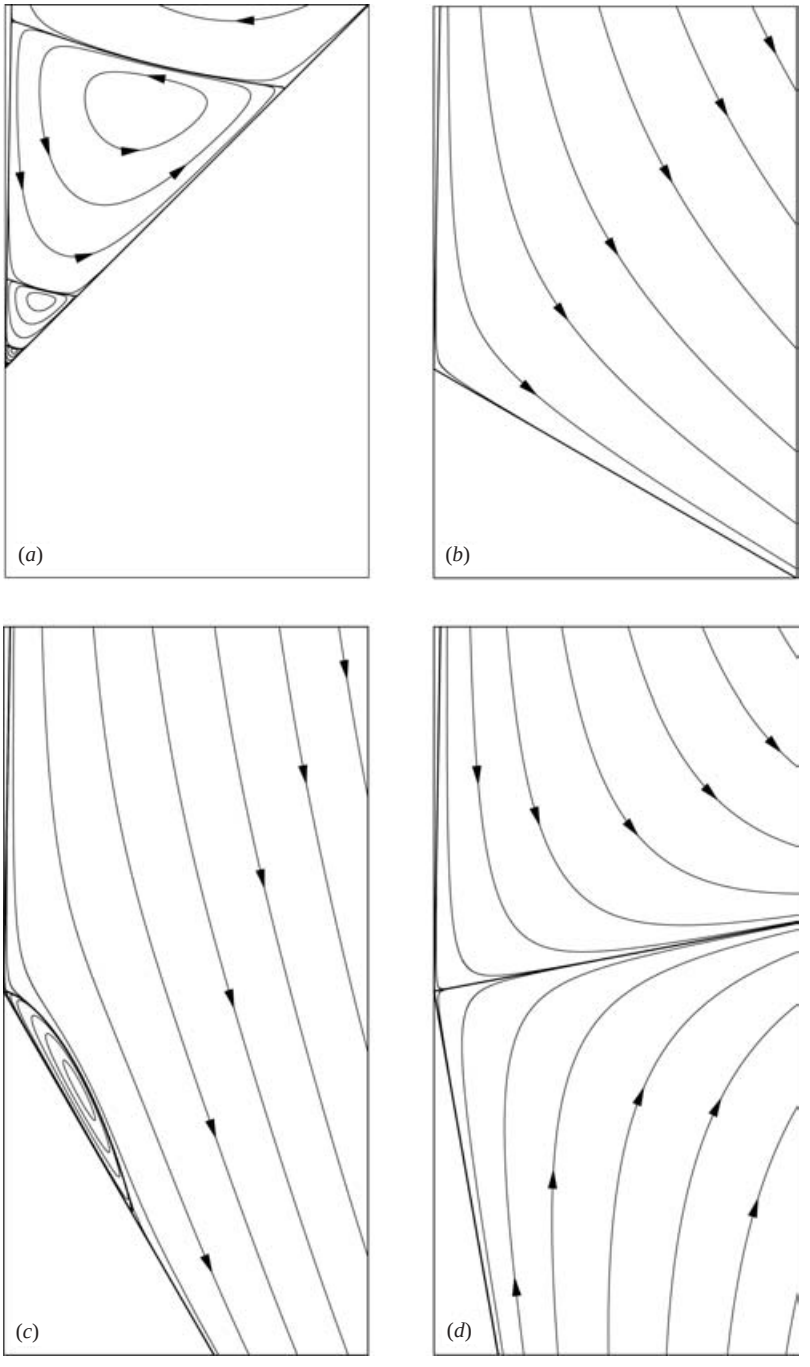

FIGURE 9. Streamline patterns computed for $\theta_1 = 1^\circ$ at the solid points in figure 8; (*a*) region (i) of nested vortices for the Re(μ_1, μ_2) eigenvalue at $\Delta\theta = 44^\circ$, (*b*) first region (ii) void of vortices for the μ_{12} eigenvalue at $\Delta\theta = 119^\circ$, (*c*) region (iii) of a single vortex anchored to the origin for the Re(μ_2, μ_3) eigenvalue at $\Delta\theta = 149^\circ$, and (*d*) second region (iv) void of vortices for μ_{12} eigenvalue at $\Delta\theta = 169^\circ$.

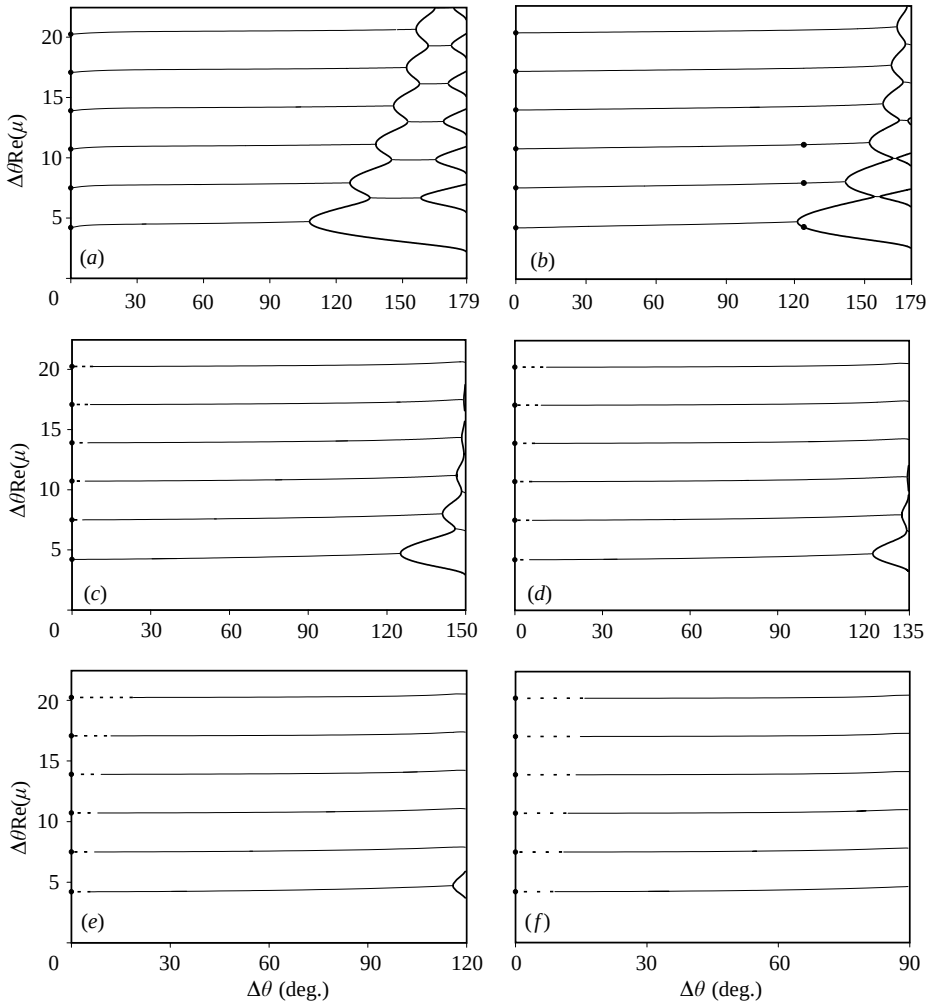

FIGURE 10. Eigenvalue spectra for (*a*) $\theta_1 = 1°$, (*b*) $\theta_1 = 10°$, (*c*) $\theta_1 = 30°$, (*d*) $\theta_1 = 45°$, (*e*) $\theta_1 = 60°$, (*f*) $\theta_1 = 90°$. The solid dots in (*b*) correspond to points where streamline patterns are plotted in figure 11.

which nested vortices disappear. We plot the variation of this and the $m = 2$, 3 and 4 critical values in figure 12(*a*). Owing to the north/south-pole symmetry, each numerically computed critical value can be used to generate an additional critical value. Specifically, for every $(\theta_2)_{c_1}$ at $(\theta_1)_1$ in the northern hemisphere, there exists the additional critical angle

$$(\theta_2)_{c_2} \to 180° - (\theta_1)_1 \qquad @ \quad (\theta_1)_2 \to 180° - (\theta_2)_{c_1}$$

in the southern hemisphere. These extra solution values generated from the numerical data listed in table 1, and similar data for $m = 2$, 3, 4, are included in figure 12(*a*). Note that for all upper cone angles $0 < \theta_1 < 90°$ the critical lower cone angles are restricted to $90° < (\theta_2)_c < 180°$. We discovered that a more informative presentation of these data is given by plotting the critical opening angle $(\Delta\theta)_c$ against the angle θ_b bisecting the fluid domain as in figure 12(*b*). This format emphasizes that nested vortices exist whenever $\Delta\theta < 90°$, as indicated by figures 4, 8 and 10, and thus the lower part of the bounding

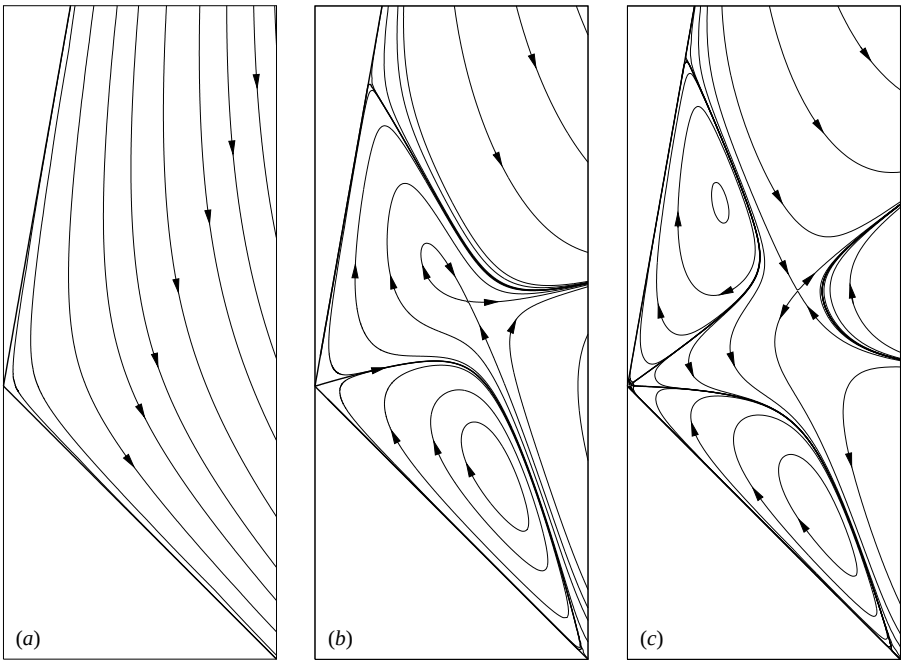

FIGURE 11. Asymmetric streamline patterns computed for $\theta_1 = 10^\circ$ and $\theta_2 = 135^\circ$ at the solid points in figure 10 (*b*) for (*a*) $m = 1$ (*b*) $m = 2$ and (*c*) $m = 3$.

θ_1	$(\theta_2)_c$	$(\Delta\theta)_c$	θ_b
0.001	92.12	92.12	46.06
0.01	94.99	94.98	47.50
0.1	99.77	99.67	49.94
1.0	108.97	107.97	54.99
5.0	122.02	117.02	63.51
10.0	131.31	121.31	70.66
20.0	144.67	124.67	82.34
27.39	152.61	125.22	90.00
30.0	155.16	125.16	92.58
45.0	167.56	122.56	106.28
60.0	175.85	115.85	117.93
70.0	178.81	108.81	124.41
85.00	179.99	94.99	132.50
87.87	179.999	92.13	133.93

TABLE 1. Calculated $m = 1$ critical angles $(\theta_2)_c$, critical opening angles $(\Delta\theta)_c$, and critical wedge bisection angles θ_b. All angles are in degrees.

triangle is omitted. The restrictions $\theta_1 > 0$, $(\theta_2)_c < 180^\circ$ imply that the envelope of critical angles $(\Delta\theta)_c$ is given by the dashed lines intersecting at $(\Delta\theta)_c = 180^\circ$, $\theta_b = 90^\circ$. It may be noted that the maximum critical angles $(\Delta\theta)_c$, plotted as open circles in figure 12(*b*), are found in the class of symmetric flows; in other words, symmetric openings support the largest opening angles for which a nested vortex structure exists. For any given θ_b, the complex modes sequentially disappear as $\Delta\theta$ increases. In the limit $\Delta\theta \to 180^\circ$ the cone pair reduces to an infinitely long, infinitesmally thin needle.

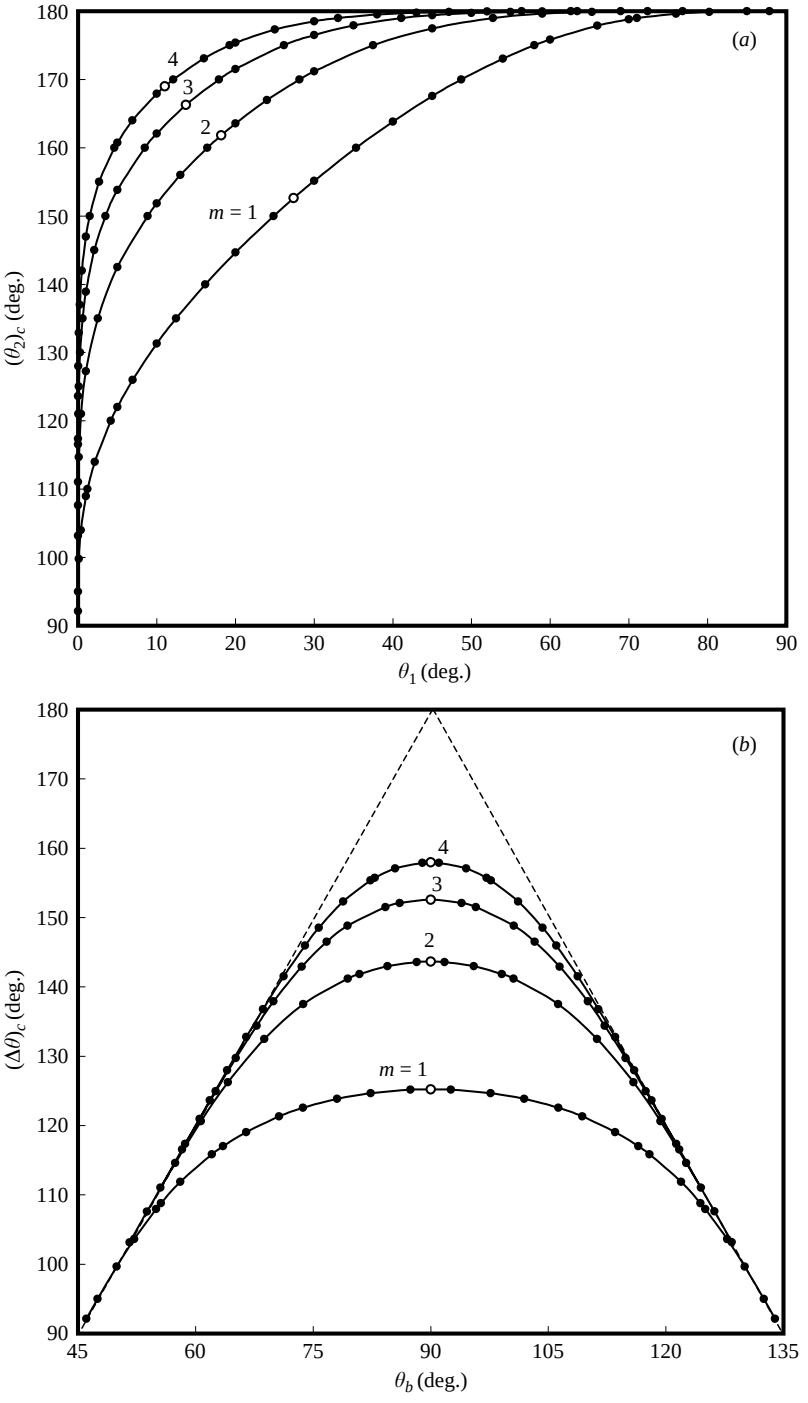

FIGURE 12. Critical angles for transition from region (i) of nested vortices to region (ii) of no vortices; (*a*) results plotted as $(\theta_2)_c$ for fixed values of θ_1, (*b*) results plotted as $(\Delta\theta)_c$ for fixed values of θ_b.

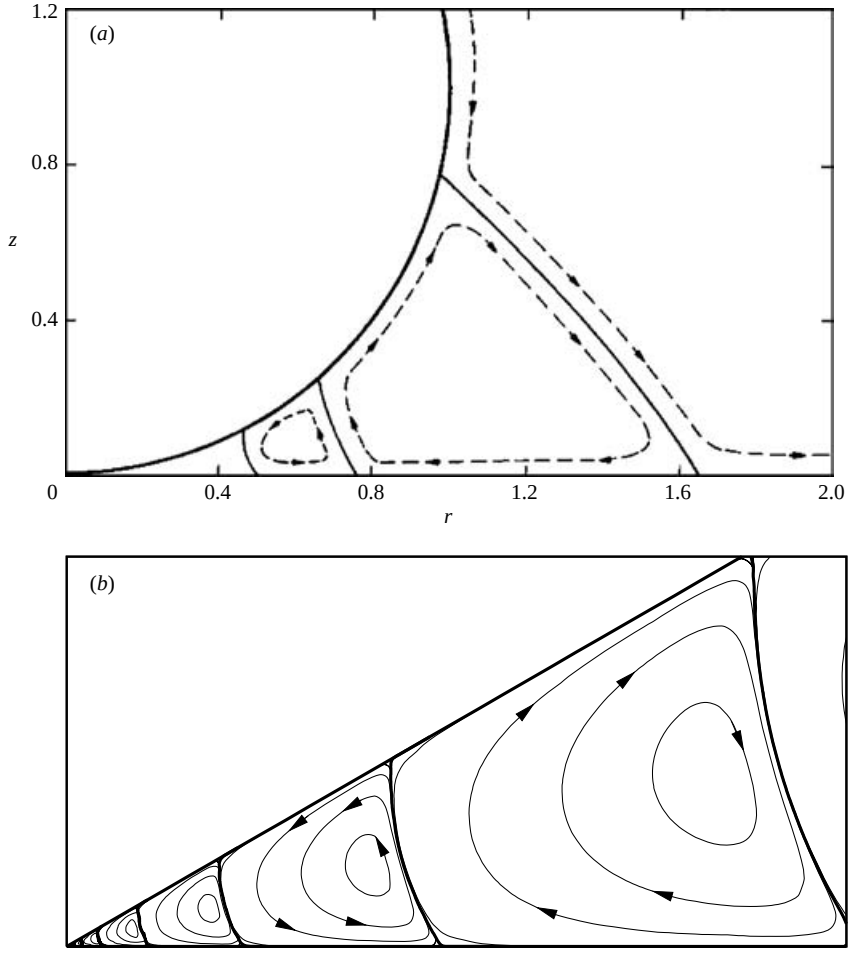

FIGURE 13. Comparison of (*a*) the sphere-on-a-wall eddy structure calculated by Davis & O'Neill (1977*a*) (reprinted with permission) with (*b*) the $m = 1$ cone-on-a-wall calculation at $\theta_1 = 60^\circ$ and $\theta_2 = 90^\circ$ of the present investigation.

Figure 13 compares an asymmetric similarity streamline pattern between cones at $\theta_1 = 60^\circ$ and $\theta_2 = 90^\circ$ that models, as pointed out in the introduction (see figure 1), the nested vortex structure of Davis & O'Neill (1977*a*) for axisymmetric stagnation flow normally impinging a sphere resting on a horizontal wall. The choice $\theta_1 = 60^\circ$ is simply a representative value of the varying angle of the sphere up to the separation streamline; any value in a neighbourhood ($\pm 10^\circ$) of 60° exhibits a similar toroidal vortex structure.

For comparison with figure 7, we show in figure 14 the morphological evolution of the free vortex for $m = 3$ for an asymmetric opening of the wedge, starting from the symmetric streamline configuration in figure 14(*a*) at $\Delta\theta = 60^\circ$ corresponding to $\theta_1 = 60^\circ$ and $\theta_2 = 120^\circ$. Subsequent frames for fixed θ_1 exhibit the streamline patterns found by increasing θ_2. As in figure 7, only a $\pm 5^\circ$ window of the flow centred on the evolving vortex is presented and the rotation of the diagonal line $\theta = \theta_b$ is geometrically accurate. The symmetric distribution of the two free stagnation circles

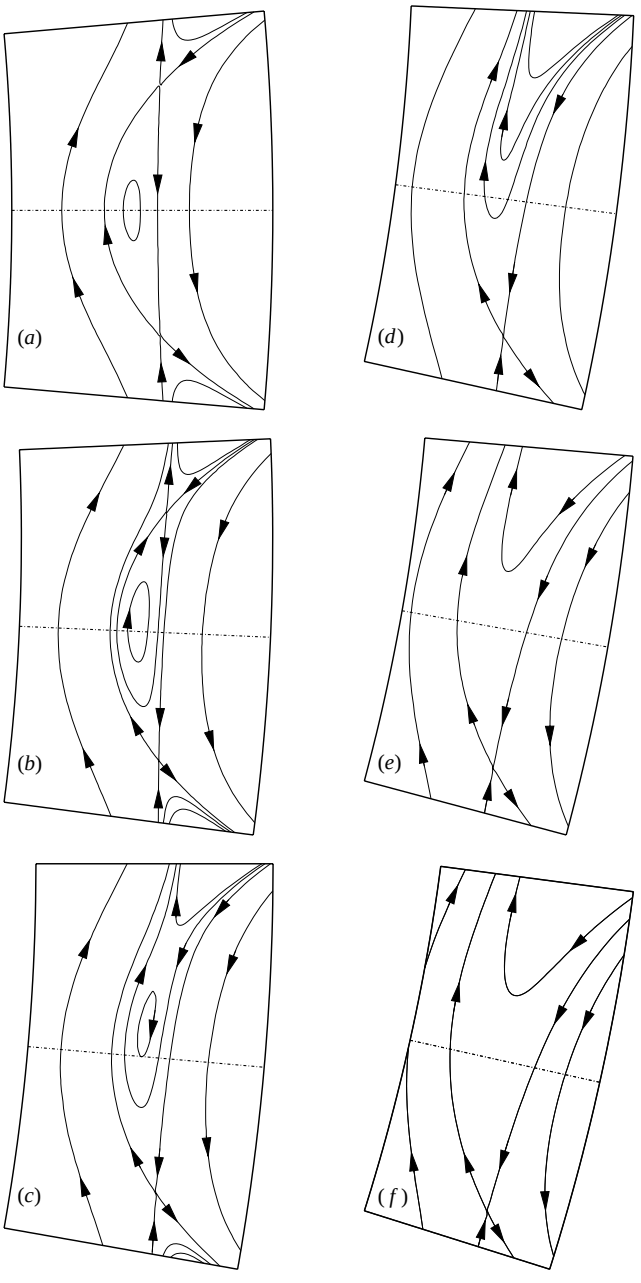

FIGURE 14. Evolution and disappearance of the free vortex for an asymmetric opening of the cones at $\theta_1 = 60°$; (*a*) $\theta_2 = 120°$, (*b*) $\theta_2 = 125°$, (*c*) $\theta_2 = 130°$, (*d*) $\theta_2 = 135°$, (*e*) $\theta_2 = 140°$, (*f*) $\theta_2 = 145°$.

defined on the same streamsurface in figure 14(*a*) immediately breaks into stagnation circles defined on different streamsurfaces in figure 14(*b*) for which $\theta_2 = 125°$. The free vortex drifts off the centreline away from the cone being opened. Both stagnation circles still exist at $\theta_2 = 130°$ in figure 14(*c*), but the upper stagnation circle and the free vortex simultaneously disappear somewhere before $\theta_2 = 135°$ in figure 14(*d*). The lower stagnation circle is maintained up to $\theta_2 = 145°$ in figure 14(*f*) and beyond.

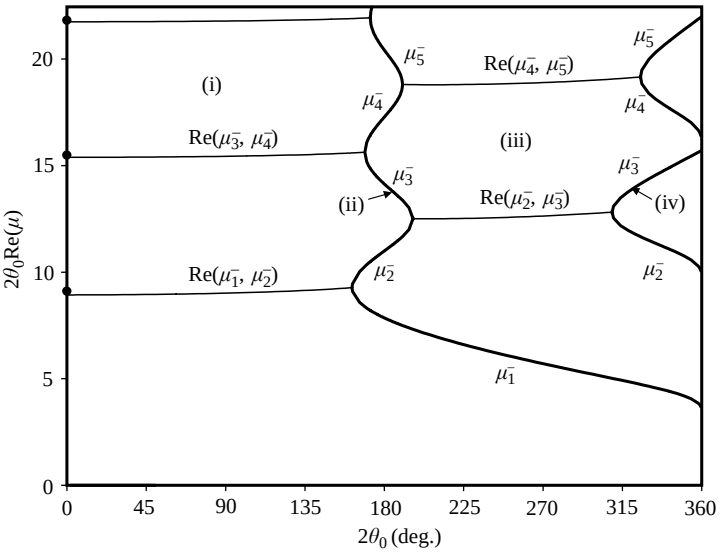

FIGURE 15. Eigenvalue distribution for flow in a conical trench showing the four regions (i), (ii), (iii) and (iv) that appear.

4. Single cone (revisited)

When dealing with flow in a cone, the Q'_μ functions, singular along the axis of symmetry $\xi = 1$, are omitted, in lieu of the conditions at θ_1 in (8), and the eigenvalue equation (9) reduces to

$$\begin{vmatrix} P'_{\mu+1/2}(\xi_2) & P'_{\mu-3/2}(\xi_2) \\ P''_{\mu+1/2}(\xi_2) & P''_{\mu-3/2}(\xi_2) \end{vmatrix} = 0. \tag{22}$$

Figure 15 displays eigenvalues on curves that closely resemble the '$-$' curves in figure 2. Counterparts to the '$+$' curves (odd modes) cannot exist because flow across the cone axis is precluded. Again, the asymptotic formulae given by Gradshteyn & Ryzhik (1994, section 8.721) can be used to estimate the limit behaviour of $z = 2\theta_0\mu$ for the conical trench as $2\theta_0 \to 0$ from the equation

$$\cos z + z = 0. \tag{23}$$

However, there is an important contrast between $\Delta\theta$, the difference between two non-zero angles, and θ_0 approaching 0 because P_μ becomes singular, in general, in the latter case. Likewise, the asymptotic analysis of Liu & Joseph requires $\mu\theta_0 \gg 1$. So, unlike the limit equation (2) for the double-cone problem, the result (23) is not exact and slight discrepancies between the computed and asymptotic values can be seen in figure 15. Consistent with the above limitation, the disparity between asymptotic and computed limit values decreases with increasing mode number: the differences are 1.98%, 0.65% and 0.32% for the $(-1,-2)$, $(-3,-4)$ and $(-5,-6)$ modes, respectively, with the asymptotic estimates always larger than the computed values.

Figure 16 displays streamlines for the lowest mode at $2\theta_0 = 60^\circ$ to compare with the streamline structure given by Liu & Joseph (their figure 1).

Our improved accuracy over their calculations can be seen for the eigenvalues listed in table 2(a) for $2\theta_0 = 20^\circ$, 60°, in table 2(b) for $2\theta_0 = 120^\circ$, 160° and in table 2(c) for

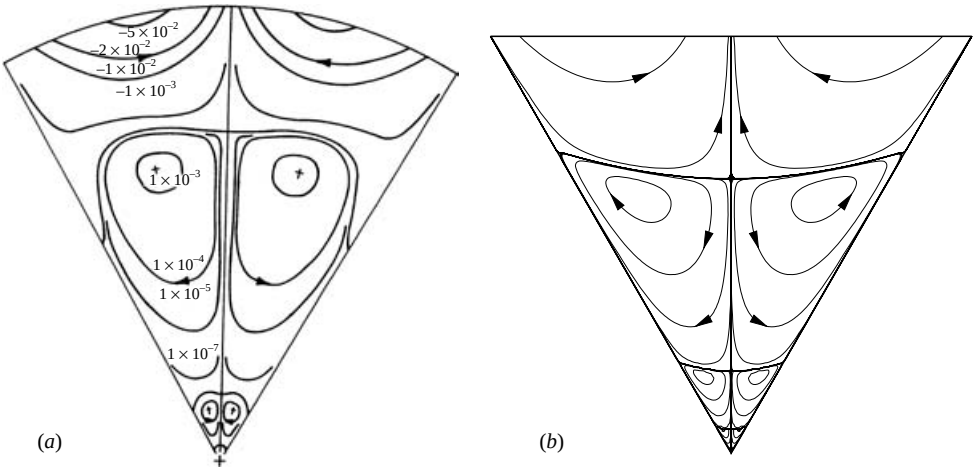

FIGURE 16. Streamline patterns for the $(-1, -2)$ mode at $2\theta_0 = 60^\circ$ comparing (a) the original figure 1 of Liu & Joseph (1978) (reprinted with permission) with (b) the present computation.

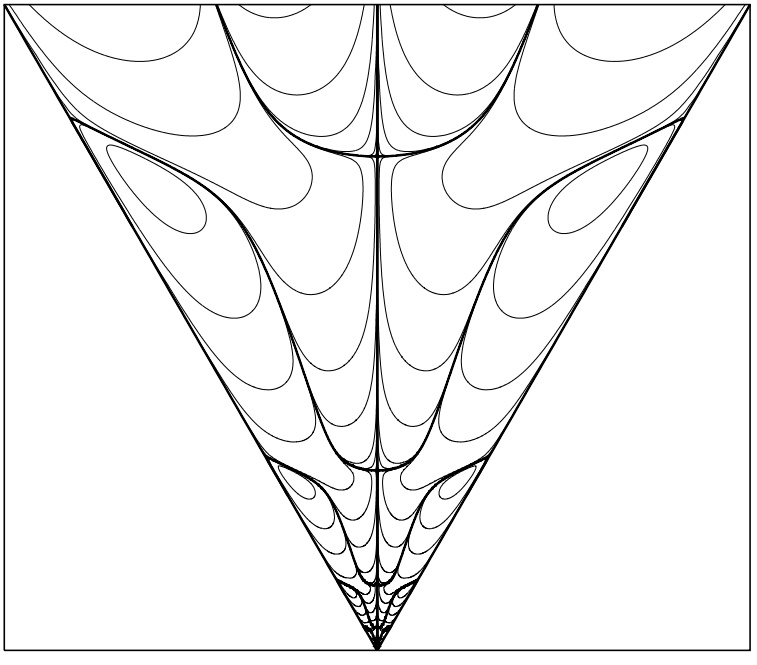

FIGURE 17. Conical-trench streamlines for mode $(-3, -4)$ with apex angle $2\theta_0 = 60^\circ$

a region (ii) value $2\theta_0 = 162^\circ$. The critical angle for disppearance of nested vortices in the lowest mode $(-1,-2)$ is computed to be $(\theta_0)_c = 80.86^\circ$, about 5° higher than the value $(\theta_0)_c = 76.95^\circ$ reported by Liu & Joseph (1978). Note, however, that our value is in accord with the critical angle 80.9° reported by Wakiya (1976).

In conclusion to this section, we note in figure 17 a striking feature of the nested vortices for the second $(-3, -4)$ mode. All toroidal vortices touch both the bounding

(*a*)	n	Complex roots $\mu_n(2\theta_0 = 20^\circ)$	n	Complex roots $\mu_n(2\theta_0 = 60^\circ)$
	1	25.601121672175 + 8.347241407096i	1	8.564202799010 + 2.613929731913i
	2	44.090488976125 + 9.835407620211i	2	14.714736394992 + 3.113756241171i
	3	62.311361125687 + 10.798240478083i	3	20.783197116510 + 3.435896144836i
	4	80.440526902464 + 11.515317446705i	4	26.823413077142 + 3.675469476171i
	5	98.526280908475 + 12.087714506945i	5	32.850196720932 + 3.866569068307i
	6	116.587765415270 + 12.564355185813i	6	38.869446025567 + 4.025633504036i
	7	134.634203492964 + 12.972814846959i	7	44.884012254987 + 4.161908430137i
	8	152.670624470004 + 13.330213887297i	8	50.895454285179 + 4.281126375624i
	9	170.700018540100 + 13.647926204919i	9	56.904700937639 + 4.387092276166i
	10	188.724281409478 + 13.933898357019i	10	62.912342123509 + 4.482462791745i
	11	206.744676169908 + 14.193903527300i	11	68.918771503280 + 4.569167063693i
	12	224.762078508565 + 14.432269079320i	12	74.924262365334 + 4.648650574494i
	13	242.777115588450 + 14.652322747119i	13	80.929010670577 + 4.722024578015i
	14	260.790248928666 + 14.856678829017i	14	86.933160776725 + 4.790161884856i
(*b*)	n	Complex roots $\mu_n(2\theta_0 = 120^\circ)$	n	Complex roots $\mu_n(2\theta_0 = 160^\circ)$
	1	4.340760366189 + 0.959888954427i	1	3.317004981782 + 0.161027196240i
	2	7.392068590616 + 1.219392026851i	2	5.581939393961 + 0.449383155228i
	3	10.416357056915 + 1.383341774381i	3	7.839775468674 + 0.587438663882i
	4	13.430972639920 + 1.504415252673i	4	10.094834614319 + 0.683958582031i
	5	16.440872106589 + 1.600660656411i	5	12.348442801215 + 0.758971056598i
	6	19.448078070582 + 1.680614723919i	6	14.601175620728 + 0.820555831985i
	7	22.453586314462 + 1.749028710927i	7	16.853331778116 + 0.872884240719i
	8	25.457949151056 + 1.808829461281i	8	19.105084490006 + 0.918418263852i
	9	28.461499558355 + 1.861951240471i	9	21.356542205627 + 0.958741575236i
	10	31.464451115407 + 1.909740445970i	10	23.607776775146 + 0.994936566448i
	11	34.466947557995 + 1.953172564427i	11	25.858837926943 + 1.027777323898i
	12	37.469089406887 + 1.992977263917i	12	28.109761300917 + 1.057837340000i
	13	40.470949208214 + 2.029714747010i	13	30.360573180679 + 1.085553712674i
	14	43.472580712861 + 2.063824544577i	14	32.611293418570 + 1.111267441113i

(*c*)	n	Complex roots $\mu_n(2\theta_0 = 162^\circ)$
	1	3.215514472031 + 0 i
	2	3.345382996720 + 0 i
	3	5.515900473320 + 0.395014239173i
	4	7.745133803130 + 0.536178915705i
	5	9.971919521537 + 0.633092385233i
	6	12.197417334119 + 0.707917365598i
	7	14.422133149018 + 0.769150236126i
	8	16.646330950008 + 0.821083498826i
	9	18.870164619328 + 0.866221024583i
	10	21.093730957655 + 0.906161834166i
	11	23.317094368558 + 0.941993577712i
	12	25.540299593652 + 0.974491491472i
	13	27.763378805747 + 1.004228511906i
	14	29.986355802133 + 1.031640506340i
	15	32.209248605147 + 1.057067027991i

TABLE 2. Fourteen first-quadrant roots of equation (22) for (*a*) $2\theta_0 = 20^\circ$, 60°, (*b*) 120°, 160° and (*c*) 162°. When $2\theta_0 = 161.72^\circ$ the first root becomes real-valued.

cone and the central axis, a feature not found in either the wedge or double-cone geometries. The same holds true for the $(-5, -6)$ and higher modes. Thus, for all conical trench modes higher than the fundamental, internal separatrices pass obliquely from the outer wall to the cone axis and are never conical.

5. Summary and conclusion

The Stokes flow bounded by two concentric coaxial cones of polar angles $\theta_2 > \theta_1$ with a common vertex allows, for the first time, consideration of the nested vortex structure in an asymmetric double-cone geometry. Our investigation reveals four flow structures, depending on the cone angles: (i) a region of nested vortices, (ii) a first region void of vortices, (iii) a region with only a solitary vortex pinned to the corner, and (iv) a second region void of vortices. Analogous flow structures exist in a wedge, but the streamline patterns in the asymmetric geometry are more intricate, especially in the higher modes. The eigenvalue plots, when scaled vertically to address the small opening angle limits, $2\theta_0$ for the wedge and $\Delta\theta$ for the double cone, have the same limits for each mode as their opening angles tend to zero.

In the symmetric double-cone configuration regions (iii) and (iv) are absent. This can be attributed to the fact that a symmetric opening about the equator is similar to the opening of a wedge from 0° to 180° and this is confirmed by the striking similarity in the flow structures for the two cases, even though the vortices are toroidal in the former case and planar in the latter. We have shown that the asymptotic distribution of eigenvalues is described by the same Moffatt (1964) equation for both even and odd flow structures in these two flows.

An interesting feature of the higher mode structures in the double-cone, single-cone, and wedge configurations is that internal separatrices in a section of the flow exhibit curvature. Mathematical analysis for the simplest wedge geometry shows that, beginning from the second odd mode, the separatrices between vortices are indeed wiggly. Another feature of interest in the streamline patterns for the second odd $(+3, +4)$ mode for the wedge and symmetric double-cone configurations is the appearance of a free central vortex sandwiched between larger wall-bounded vortices. On opening the two bounding cones beyond approximately 87° the free vortex collapses into a free stagnation circle at the equator.

Though the second mode is typically $O(10^{-3})$ weaker than the fundamental, it can appear naturally in a properly devised experiment. Consider a sphere with a symmetric equatorial opening, filled with silicone oil seeded with tiny polystryrene spheres and with density matching that of water, placed inside a cylinder, with sphere polar axis and cylinder axis aligned. Water forced through a porous annular section of the cylinder centred on the sphere would impinge on the sphere as a local axisymmetric radial stagnation flow and leave the cylinder through opposing ends. The symmetric external forcing of the immiscible oil in the axisymmetric wedge of the sphere would induce a nested symmetric $(-1, -2)$ mode vortex structure of the kind shown in figure 5(*b*). Since there is no forcing by the fundamental mode, the outermost vortex pair would be readily visible and, using long-time-exposure photography following Taneda (1979), the second vortex pair should be visible as well.

While the symmetrically opening double cone mimics a wedge opening to 180°, asymmetrically opening cones with opening angles greater than 90° are akin to a wedge with an opening angle greater than 180° with eigenvalues lying in regions (iii) and (iv) where nested vortices are absent. Following the evolution of the double-cone eigenplots with increasing values of upper cone angle θ_1 suggests that regions (iii) and (iv) disappear when $\theta_1 \gtrsim 60^\circ$. However, based on symmetry considerations, it can be shown that these regions do exist for $\Delta\theta > 90^\circ$ in a tiny region adjacent to $\theta_2 = 180^\circ$ where the lower cone becomes a needle.

New computations correcting the results of Liu & Joseph (1978) for Stokes flow in a conical trench are presented. We find that the critical value for disappearance of the

nested vortex structure in the lowest mode changes from $\theta_0 = 76.95^\circ$ to $\theta_0 = 80.86^\circ$, and thus the region of existence of nested vortices is larger than anticipated by those authors. Our computation for the critical angle is in agreement with the value 80.9° reported by Wakiya (1976). In this geometry, the internal separatrices between the toroidal vortices, for all modes above the fundamental, traverse obliquely from the cone wall to the cone axis.

The final manuscript benefits from comments and suggestions provided by three referees and the editor. In particular, we are indebted to a referee who pointed out an important reference missing from our bibliography. The lead author greatly appreciates the support extended by Tata Research Development and Design Centre through its director, Professor Mathai Joseph.

REFERENCES

Betelú, S., Diez, J., Gratton, J. & Thomas, L. 1996 Instantaneous flow in a corner bounded by free surfaces. *Phys. Fluids* **8**, 2269–2274.

Davis, A. M. J. 1989 Thermocapillary convection in liquid bridges: Solution structure and eddy motions. *Phys. Fluids* A **1**, 475–479.

Davis, A. M. J. & O'Neill, M. E. 1977*a* The development of viscous wakes in a Stokes flow when a particle is near a large obstacle. *Chem. Engng Sci.* **32**, 899–906.

Davis, A. M. J. & O'Neill, M. E. 1977*b* Separation in a slow linear shear flow past a cylinder and a plane. *J. Fluid Mech.* **81**, 551–564.

Dean, W. R. & Montagnon, P. E. 1949 On the steady motion of a viscous liquid in a corner. *Proc. Camb. Phil. Soc.* **45**, 389–394.

Gradshteyn, I. S. & Ryzhik, I. M. 1994 *Tables of Integrals, Series and Products*, 5th Edn. Academic.

Kuhlmann, H. C., Nienhüser, C. & Rath, H. J. 1999 The local flow in a wedge between a rigid wall and a surface of constant shear stress. *J. Engng Maths* **36**, 207–218.

Liu, C. H. & Joseph, D. D. 1978 Stokes flow in conical trenches. *SIAM J. Appl. Maths* **34**, 286–296.

Moffatt, H. K. 1964 Viscous and resistive eddies near a sharp corner. *J. Fluid Mech.* **18**, 1–18.

Moffatt, H. K. & Duffy, B. R. 1980 Local similarity solutions and their limitations. *J. Fluid Mech.* **96**, 299–313.

Taneda, S. 1979 Visualization of separating Stokes flows. *J. Phys. Soc. Japan* **46**, 1935–1942. See also *An Album of Fluid Motion* (ed. M. Van Dyke). The Parabolic Press, Stanford, 1982.

Wakiya, S. 1976 Axisymmetric flow of a viscous fluid near the vertex of a body. *J. Fluid Mech.* **78**, 737–747.

Weidman, P. D. & Calmidi, V. 1999 Instantaneous Stokes flow in a conical apex aligned with gravity and bounded by a stress-free surface. *SIAM J. Appl. Maths* **59**, 1520–1531.

Wolfram, S. 1991 *Mathematica: A System for Doing Mathematics by Computer*, 2nd edn. Addison-Wesley, Redwood City.